

Attention-Enhanced Neural Network Models for Turbulence Simulation

Wenhui Peng (彭文辉)^{1,2,3,4}, Zelong Yuan (袁泽龙)^{1,2,3} and Jianchun Wang (王建春)^{1,2,3}

¹⁾*Department of Mechanics and Aerospace Engineering, Southern University of Science and Technology, Shenzhen 518055, China*

²⁾*Southern Marine Science and Engineering Guangdong Laboratory (Guangzhou), Guangzhou 511458, China*

³⁾*Guangdong-Hong Kong-Macao Joint Laboratory for Data-Driven Fluid Mechanics and Engineering Applications, Southern University of Science and Technology, Shenzhen 518055, China*

⁴⁾*Department of Computer Engineering, Polytechnique Montreal, H3T1J4, Canada*

(*Electronic mail: wangjc@sustech.edu.cn)

(Dated: 7 January 2022)

Deep neural network models have shown a great potential in accelerating the simulation of fluid dynamic systems. Once trained, these models can make inference within seconds, thus can be extremely efficient. However, it becomes more difficult for neural networks to make accurate predictions when the flow becomes more chaotic and turbulent at higher Reynolds numbers. One of the most important reasons is that, existing models lack the mechanism to handle the unique characteristic of high-Reynolds-number turbulent flow: multi-scale flow structures are non-uniformly distributed and strongly nonequilibrium. In this work, we address this issue with the concept of visual attention: intuitively, we expect the attention module to capture the nonequilibrium of turbulence by automatically adjusting weights on different regions. We compare the model performance against a state-of-the-art neural network model as baseline, the Fourier Neural Operator (FNO), on two-dimensional (2D) turbulence prediction task. Numerical experiments show that the attention-enhanced neural network model outperforms existing state-of-the-art baselines, and can accurately reconstruct a variety of statistics and instantaneous spatial structures of turbulence at high Reynolds numbers flow. Furthermore, the attention mechanism provides 40% error reduction with 1% increase of parameters, at the same level of computational cost.

I. INTRODUCTION

Over the past few years, data-driven approaches based on machine learning (ML) have been extensively explored to complement and accelerate traditional computational fluid dynamics methods^{1,2}. Most of them follows two routes: ML-assisted model-driven approaches and pure data-driven approaches. The ML-assisted model-driven approaches aim to fit the closures of classical turbulence models based on consistency with high-resolution direct numerical simulations. Ling et al. presented a method of using deep neural networks to learn a model for the Reynolds stress anisotropy tensor from high fidelity simulation data³. Maulik et al. used neural networks to learn the map between inputs given by stencils of the vorticity and the streamfunction along with information from the eddy-viscosity kernels, and predict the sub-grid vorticity forcing in a temporally and spatially dynamic fashion⁴. Wang et al. introduced a semi-explicit deep learning based framework for the reconstruction of the subgrid-scale stress in the large eddy simulation of incompressible turbulence⁵. Beck et al. designed networks based on local convolution filters to predict the underlying unknown non-linear mapping from the coarse grid quantities to the closure terms without prior assumptions⁶. Portwood et al. showed that artificial neural networks can provide useful insights in the process of developing and improving turbulence closures⁷. Park et al. used a fully connected neural network to develop a subgrid-scale (SGS) model in a turbulent channel flow⁸. Yuan et al. developed a dynamic iterative approximate deconvolution models with Galilean invariance for the subgrid-scale stress in the large-eddy simulation of turbulence⁹.

Despite that the ML-assisted models are potentially more accurate than traditional turbulence models, they failed to achieve the desired computational expense reduction¹⁰. By contrast, the pure data-driven methods aim to approximate the entire Navier-Stokes equations by deep neural networks¹¹⁻¹⁴. Once trained, the "black-box" neural network models can make inference within seconds on modern computers, thus can be extremely efficient compared with traditional approaches¹⁵.

Jin et al. proposed a fusion convolutional neural networks using measurements of the pressure field on the cylinder to predict the velocity field around a cylinder¹⁶. Sekar et al. presented a data driven approach that combines the deep convolution neural network and deep multilayer perceptron to predict the incompressible laminar steady flow field over airfoils¹⁷. Chen et al. proposed to apply the U-net architectures for fast prediction in laminar flows¹⁸. Cheng et al. used the deep residual neural network to predict the flow velocity fields¹⁹. Yousif et al. applied the generative adversarial network to reconstruct high-resolution turbulent flow fields²⁰. Chen et al. proposed a graph neural networks architecture as a surrogate model for laminar flow prediction around two-dimensional obstacles²¹. Schmidt et al. simulated the turbulence quantities with a deep neural network to accelerate the modeling of transient flashing jets²². Han et al. designed a hybrid deep neural network architecture to capture the spatial-temporal features of unsteady flows from the high-dimensional numerical unsteady flow field²³. Nakamura et al. presented a machine learning based reduced order model for three-dimensional complex flows, by combining a three-dimensional convolution neural network autoencoder and a long short-term memory network. Wang et al. developed a convolution neural

network to improve the near-wall velocity field prediction²⁴. Li et al. proposed a deep neural network architecture for reconstructing the slices of the two-dimensional pressure field in three-dimensional flow, where the architecture embeds the convolution into the long short-term memory network to realize the purpose of using the upstream pressure to reconstruct downstream pressure²⁵. Ren et al. proposed a deep learning framework that combines the long short-term memory network and the convolution neural network for prediction of temporal evolution of turbulent flames²⁶.

Despite these significant achievements in the acceleration of flow simulation, these models suffer from the generalization problem, and are sensitive to the parameters change¹⁰. Recent progress has been made to relieve the generalization problem with prior physical knowledge²⁷. Erichson et al. proposed to include the physics-informed prior knowledge to improve the model generalization performance on a fluid flow prediction task²⁸. Pawar et al. developed a physics-guided machine learning framework that leverages the interpretable physics-based model with a deep learning model, to improve the generalizability of neural networks²⁹. Xu et al. employed the physics-informed deep learning by treating the governing equations as a parameterized constraint to reconstruct the missing flow dynamics³⁰. Wang et al. further applied the physical constraints into the design of neural network, and proposed a grounded in principled physics model: the turbulent-flow network (TF-Net). The architecture of TF-Net contains trainable spectral filters in a coupled model of Reynolds-averaged Navier-Stokes simulation and large eddy simulation, followed by a specialized U-net for prediction. The TF-Net offers the flexibility of learned representations, and achieved state-of-the-art prediction accuracy³¹.

Proposed by Li et al., the Fourier neural operator (FNO) mimics the pseudo-spectral methods^{32,33}: it parameterizes the integral kernel in the Fourier space, thus directly learns the mapping from any functional parametric dependence to the solution³⁴. Benefited from the expressive and efficient architecture, the FNO outperforms previous state-of-the-art neural network models: the FNO achieves 1% error rate on two-dimensional (2D) turbulence prediction task at low Reynolds numbers. However, when the fluid dynamic system becomes more chaotic, the Fourier neural operator suffers from the same problem³⁴: the error rate arises over 15% at the Reynolds number of 10^5 .

Making accurate predictions of turbulence at high Reynolds numbers has always been a difficult and challenging task for neural networks. An import reason is that the existing neural network models fail to efficiently incorporate the multi-scale and nonequilibrium characteristics of the high Reynolds numbers turbulence into the design of network architecture.

We propose to model the multi-scale and chaotic properties of turbulence with the concept of visual attention. Human visual attention allows us to focus on a specific region that contains important features while perceiving the surrounding environment with less concentration. Inspired by the human visual attention, we expect the attention mechanism to capture strongly nonequilibrium regions by focusing on certain important regions in the flow field.

The attention mechanism in deep learning was first introduced by Bahdanau et al. for machine translation³⁵. In recent years, attention mechanism has shown itself to be very successful in boosting the performance of neural networks on a variety of tasks, ranging from nature language processing to computer vision³⁶⁻³⁸. In fluid dynamics, attention mechanism has also been used to enhance the reduced order model to extract temporal feature relationships from high-fidelity numerical solutions³⁹. In this work, we couple the attention mechanism with the state-of-the-art FNO model to improve the model performance on high Reynolds numbers flow.

This paper is organized as follow: section II briefly introduces the Fourier neural operator, section III shows the detailed implementation of the attention mechanism, in section IV we benchmark the attention improvement with numerical experiments on the prediction task of 2D turbulence. In the sections V and VI we give discussions and draw conclusions, respectively.

II. THE FOURIER NEURAL OPERATOR

Most neural network architectures have focused on learning mappings between finite-dimensional Euclidean spaces, they are good at learning a single instance of the equation, but have difficulty to generalize well once the governing equation parameters or boundary conditions changes^{27,40-42}. Given a finite collection of the observed input-output pairs, the Fourier neural operator learns the mapping from any functional parametric dependence to the solution, meaning that they learn an entire family of partial differential equations instead of a single equation³⁴. Specifically, let $D \subset \mathbb{R}^d$ be a bounded, open set, and notate the target non-linear mapping as $G^\dagger : \mathcal{A} \rightarrow \mathcal{U}$, where $\mathcal{A} (D; \mathbb{R}^{d_a})$ and $\mathcal{U} (D; \mathbb{R}^{d_u})$ are separable Banach spaces of function taking values in \mathbb{R}^{d_a} and \mathbb{R}^{d_u} respectively⁴³. The Fourier neural operators learns an approximation of G^\dagger by constructing a mapping parameterized by $\theta \in \Theta$.

$$G : \mathcal{A} \times \Theta \rightarrow \mathcal{U}.$$

The optimal parameters $\theta^\dagger \in \Theta$ are determined in the test-train setting by using a data-driven empirical approximation⁴⁴, such that $G(\cdot, \theta^\dagger) = G_{\theta^\dagger} \approx G^\dagger$.

The neural operators¹⁵ are formulated as an iterative architecture $v_0 \mapsto v_1 \mapsto \dots \mapsto v_T$ where v_j for $j = 0, 1, \dots, T-1$ is a sequence of functions each taking values in \mathbb{R}^{d_v} , as shown in Fig.1. Firstly, the input $a \in \mathcal{A}$ is transformed to a higher dimensional representation

$$v_0(x) = P(a(x)).$$

by a fully connected layer P , then the higher dimensional representation is updated iteratively by Eq.(1), where $\mathcal{K} : \mathcal{A} \times \Theta_{\mathcal{K}} \rightarrow \mathcal{L}(\mathcal{U}(D; \mathbb{R}^{d_v}), \mathcal{U}(D; \mathbb{R}^{d_v}))$ maps to bounded linear operators on $\mathcal{U}(D; \mathbb{R}^{d_v})$ and is parameterized by $\phi \in \Theta_{\mathcal{K}}$, $W : \mathbb{R}^{d_v} \rightarrow \mathbb{R}^{d_v}$ is a linear transformation, and $\sigma : \mathbb{R} \rightarrow \mathbb{R}$ is an elementally defined non-linear activation function. Lastly, the

output $u \in \mathcal{U}$ is obtained by applying the local transformation $u(x) = Q(v_T(x))$, where $Q: \mathbb{R}^{d_v} \rightarrow \mathbb{R}^{d_u}$.

$$v_{t+1}(x) = \sigma(Wv_t(x) + (\mathcal{K}(a; \phi)v_t)(x)), \quad \forall x \in D. \quad (1)$$

Let \mathcal{F} and \mathcal{F}^{-1} denote the Fourier transform and its inverse transform of a function $f: D \rightarrow \mathbb{R}^{d_v}$ respectively. Replacing the kernel integral operator in Eq. (1) by a convolution operator defined in Fourier space, and applying the convolution theorem, the Fourier integral operator can be expressed by Eq.(2), where R_ϕ is the Fourier transform of a periodic function $\kappa: \bar{D} \rightarrow \mathbb{R}^{d_v \times d_v}$ parameterized by $\phi \in \Theta_{\mathcal{K}}$, as shown in Fig.1.

$$(\mathcal{K}(\phi)v_t)(x) = \mathcal{F}^{-1}(R_\phi \cdot (\mathcal{F}v_t))(x), \quad \forall x \in D. \quad (2)$$

The frequency mode $k \in D$ is assumed to be periodic, and it allows a Fourier series expansion, which expresses as the discrete modes $k \in \mathbb{Z}^d$. The finite-dimensional parameterization is implemented by truncating the Fourier series at a maximal number of modes $k_{\max} = |\mathbb{Z}_{k_{\max}}| = |\{k \in \mathbb{Z}^d: |k_j| \leq k_{\max, j}, \text{ for } j = 1, \dots, d\}|$. We discretize the domain D with $n \in \mathbb{N}$ points, where $v_t \in \mathbb{R}^{n \times d_v}$ and $\mathcal{F}(v_t) \in \mathbb{C}^{n \times d_v}$. R_ϕ is parameterized as complex-valued weight tensor containing a collection of truncated Fourier modes $R_\phi \in \mathbb{C}^{k_{\max} \times d_v \times d_v}$, and $\mathcal{F}(v_t) \in \mathbb{C}^{k_{\max} \times d_v}$ is obtained by truncating the higher modes, therefore

$$(R_\phi \cdot (\mathcal{F}v_t))_{k,l} = \sum_{j=1}^{d_v} R_{\phi k,l,j} (\mathcal{F}v_t)_{k,j}, \\ k = 1, \dots, k_{\max}, \quad j = 1, \dots, d_v.$$

In CFD modeling, the flow is typically uniformly discretized with resolution $s_1 \times \dots \times s_d = n$, and \mathcal{F} can be replaced by the Fast Fourier Transform (FFT). For $f \in \mathbb{R}^{n \times d_v}$, $k = (k_1, \dots, k_d) \in \mathbb{Z}_{s_1} \times \dots \times \mathbb{Z}_{s_d}$, and $x = (x_1, \dots, x_d) \in D$ the FFT $\hat{\mathcal{F}}$ and its inverse $\hat{\mathcal{F}}^{-1}$ are given by Eq. (3), for $l = 1, \dots, d_v$.

$$(\hat{\mathcal{F}}f)_l(k) = \sum_{x_1=0}^{s_1-1} \dots \sum_{x_d=0}^{s_d-1} f_l(x_1, \dots, x_d) e^{-2i\pi \sum_{j=1}^d \frac{x_j k_j}{s_j}}. \\ (\hat{\mathcal{F}}^{-1}f)_l(x) = \sum_{k_1=0}^{s_1-1} \dots \sum_{k_d=0}^{s_d-1} f_l(k_1, \dots, k_d) e^{2i\pi \sum_{j=1}^d \frac{x_j k_j}{s_j}}. \quad (3)$$

III. ATTENTION-ENHANCED NEURAL NETWORK

Human visual attention allows us to focus on a specific region that contains important features while perceiving the surrounding environment with less concentration. Inspired by the concept of visual attention, we propose to model the nonequilibrium features of turbulence with the self-attention module in machine vision⁴⁵.

The idea of attention mechanism was first popularly applied in the domain of natural language processing³⁶. An attention function can be described as mapping a query and a set of key-value pairs to an output, where the query, keys, values, and output are all vectors. The output is computed as a weighted sum of the values, where the weight assigned to each value is computed by a compatibility function of the query with the corresponding key³⁶. The three sub-modules (query, key, and value) are the pivotal components of attention mechanism, which come from the concepts of information retrieval systems⁴⁶. An example is the query search, where the search engine maps the query to a set of keys, and output the values. Zhang et al. extended the idea into the domain of computer vision by proposing the self-attention module⁴⁵. The overall architecture of the self-attention block is shown in Fig.2, it learns sequential attention maps that are called the channel attention and the space attention. The first layer performs 1×1 convolutions on $v_t(x)$ to sequentially infer the channel attention map \mathbf{M}_c and the space attention map \mathbf{M}_s , as shown in Eq.4. The self-attention operation mimics the "proportional retrieval" approach from information retrieval systems, where s_{ij} corresponds to the probability vector⁴⁶.

$$\mathbf{M}_c = W_h v_t(x), \\ \mathbf{M}_s = \frac{\exp(s_{ij})}{\sum_{i=1}^N \exp(s_{ij})},$$

$$\text{where } s_{ij} = (W_f v_t(x_i))^T (W_g v_t(x_j)). \quad (4)$$

The convolution parameters W_f, W_g, W_h learn the embedding of query, key and value, respectively. Eq. 5 gives the attention refined feature maps, where \otimes denotes the dot product.

$$v_t(x)' = \mathbf{M}_s \otimes \mathbf{M}_c. \quad (5)$$

The sequence of functions $v_0 \mapsto v_1 \mapsto \dots \mapsto v_T$ is the core structure of Fourier network, which directly affects the model learning capability. In the original network, $v_t \mapsto v_{t+1}$ is updated by Eq. 1, and we use the self-attention block to refine the FNO output as feature augmentation as shown in Fig.3. The self-attention block takes the feature maps of Fourier neural operators $v_t(x)$ as input, and output the attention refined feature maps $v_t(x)'$.

Despite that the self-attention module allows feature refinement for any neural operators $v_t \Rightarrow v_t'$ for $t = 1, \dots, T$, our numerical experiments show that a single block at the end of sequence $v_T \Rightarrow v_T'$ has the same level of improvement as refining all neural operators in the sequence $v_1 \Rightarrow v_1' \mapsto \dots \mapsto v_T \Rightarrow v_T'$.

The attention parameters W_f, W_g, W_h can be jointly learned with the Fourier layer during training. More importantly, since the attention block adopts 1×1 convolution filters, it retains the mesh invariant property of neural operators, meaning that the attention-enhanced FNO still keeps the ability of training on coarse grid and making inference on finer grid without seeing any higher resolution data. Details are discussed in Sec. IV D.

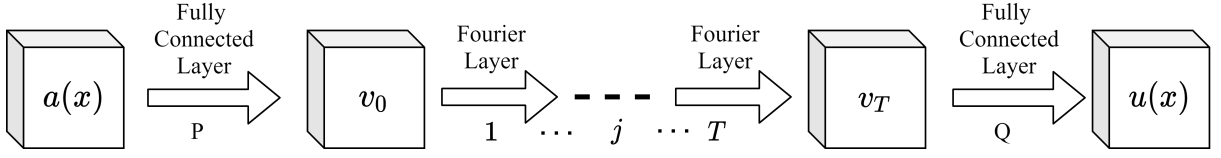


FIG. 1: Fourier neural operator (FNO) architecture.

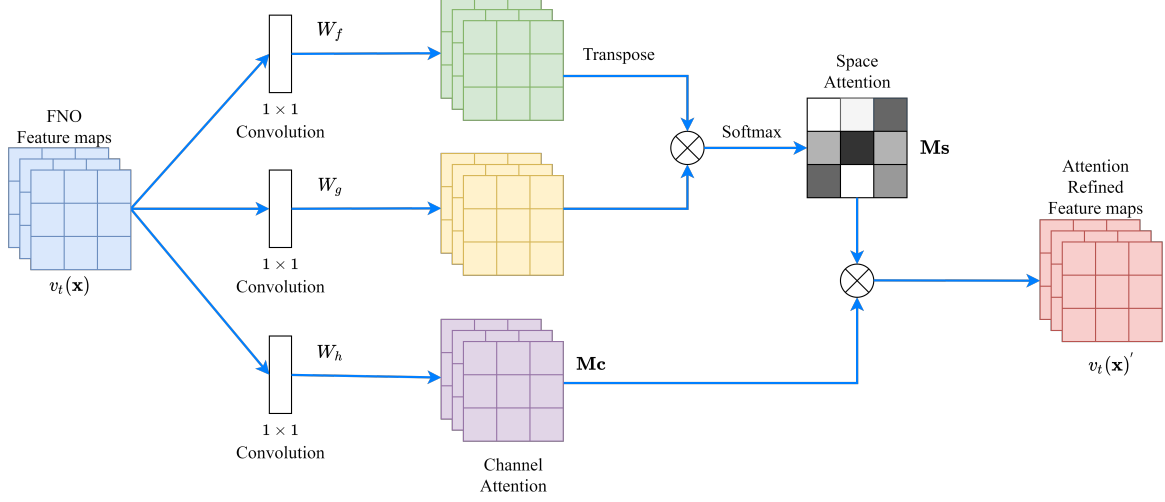


FIG. 2: Self-attention block.

IV. PERFORMANCE BENCHMARK

In this section, we benchmark the performance of attention-augmented neural network against the original FNO model with various criteria, including the vorticity prediction error, the vorticity spectrum, the probability density function (PDF) for vorticity and the condition average error of the vorticity. We conduct numerical experiments to evaluate the prediction ability of the two models (FNO, FNO+Attention) on the same dataset of 2D incompressible turbulence with reference³⁴. The numerical experiments are implemented on the Pytorch and MindSpore deep learning frameworks. We also compare the performance of two models on more complex turbulent flows: the Taylor-Green turbulence and free shear turbulence. Specifically, we are interested in comparing the prediction accuracy of the two models at different time steps and at different Reynolds numbers.

A. Dataset description

Eq. (6) describes the dimensionless Navier-Stokes equations for a viscous, incompressible fluid on the unit torus, where $u \in C([0, T]; H_{\text{per}}^r((0, 1)^2; \mathbb{R}^2))$ for any $r > 0$ is the velocity field, $\omega = \nabla \times \mathbf{u}$ is the vorticity, $\omega_0 \in L_{\text{per}}^2((0, 1)^2; \mathbb{R})$ is the initial vorticity, Re is the Reynolds number, and $f \in L_{\text{per}}^2((0, 1)^2; \mathbb{R})$ is the forcing function.

$$\begin{aligned} \partial_t \omega(\mathbf{x}, t) + \mathbf{u}(\mathbf{x}, t) \cdot \nabla \omega(\mathbf{x}, t) &= (1/Re)\Delta \omega(\mathbf{x}, t) + f(\mathbf{x}), \\ \omega(\mathbf{x}, t) &= \omega_0(\mathbf{x}), \\ \mathbf{x} &\in (0, 1)^2, t \in [0, T]. \end{aligned} \quad (6)$$

The initial condition $\omega_0(\mathbf{x})$ is generated according to $\omega_0 \sim \mu$ with periodic boundary conditions³⁴, where the Gaussian random distribution $\mu = \mathcal{N}(0, 7^{3/2}(49 - \Delta)^{-2.5})$ is expressed as

$$\mu(\mathbf{x}) = \frac{1}{2\pi \times 7^3 (49 - \Delta)^{-5}} \exp\left[-\frac{x_1^2 + x_2^2}{2 \times 7^3 (49 - \Delta)^{-5}}\right]. \quad (7)$$

Here, $\Delta = 2\pi/N$ represents the uniform grid spacing.

Fig. 4 shows the initial vorticity of ten random conditions, which are sampled from the training set and the testing set. The forcing is kept fixed $f(\mathbf{x}) = 0.1 [\sin(2\pi(x_1 + x_2)) + \cos(2\pi(x_1 + x_2))]$.

In this paper, a pseudo-spectral method is applied to numerically simulate the incompressible 2D homogeneous isotropic turbulence in a cubic box of $(2\pi)^2$ on a uniform grid with periodic boundary conditions. The vorticity can be expanded as the Fourier series,

$$\omega(\mathbf{x}, t) = \sum_{\mathbf{k}} \hat{\omega}(\mathbf{k}, t) \exp(i\mathbf{k} \cdot \mathbf{x}), \quad (8)$$

where i stands for the imaginary unit, namely, $i^2 = -1$, $\mathbf{k} = [k_x, k_y]^T$ is the wavenumber vector, and the superscript “ $\hat{\cdot}$ ” represents the variable in Fourier space. The vorticity equation in

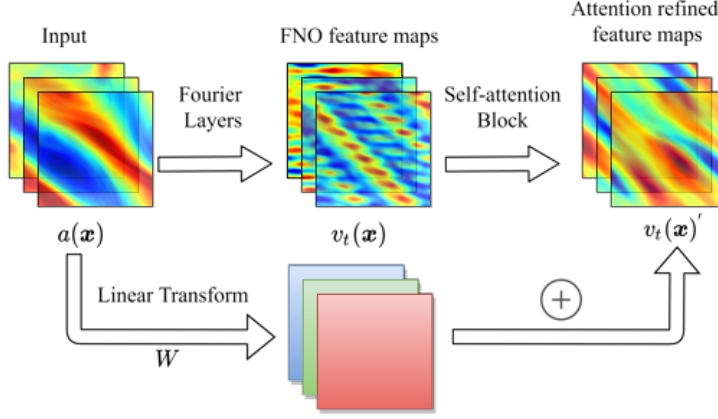


FIG. 3: Attention enhanced Fourier neural operator (FNO).

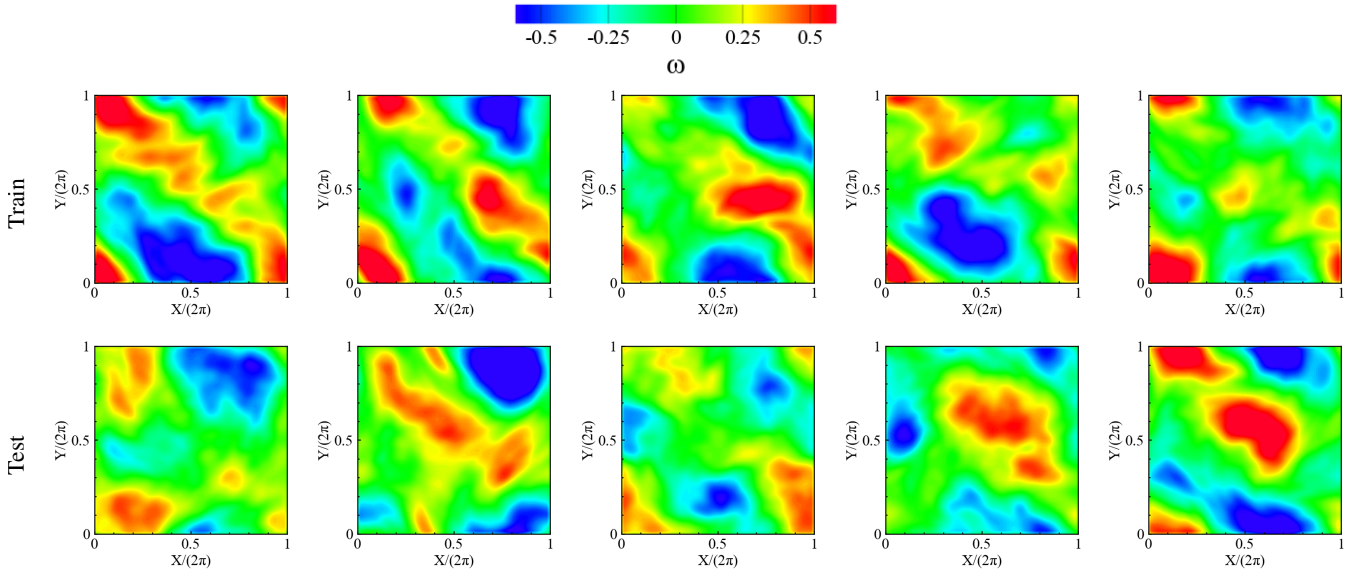


FIG. 4: Random sampled initial conditions from the training set and testing set.

wavenumber space can be derived as

$$\left(\frac{d}{dt} + \frac{1}{\text{Re}} k^2 \right) \hat{\omega}(\mathbf{k}, t) = \hat{f}(\mathbf{k}, t) - \mathbf{u}(\mathbf{x}, t) \bullet \widehat{\nabla \omega}(\mathbf{x}, t), \quad (9)$$

The nonlinear advection term is calculated by the pseudo-spectral method³⁴. The basic procedure is to first transform the Fourier variables $\hat{\mathbf{u}}(\mathbf{k}, t) = [-ik_y \hat{\omega}/k^2, ik_x \hat{\omega}/k^2]^T$ and $\hat{\omega}(\mathbf{k}, t)$ to $\mathbf{u}(\mathbf{x}, t)$ and $\nabla \omega(\mathbf{x}, t)$ in physical space by the inverse fast Fourier transform, and perform the multiplication in physical space to obtain $\mathbf{u}(\mathbf{x}, t) \bullet \nabla \omega(\mathbf{x}, t)$, after that the forward fast Fourier transform is calculated and aliasing error is removed by the 3/2 zero-padding rule³⁴, respectively. Data are generated on the grid size of 256×256 and are downsampled to 64×64 . Time is advanced with the Crank-Nicolson scheme, where the time-step is set to be 10^{-4} , and the solution is recorded every $t = 1$ time units. An explicit two-step Adams-Bashforth scheme is selected as the time marching

scheme with second-order temporal accuracy. For a partial differential equation $\partial_t \hat{\omega} = R(\hat{\omega}, t)$, the iterative scheme for time advancement is given by Eq. 10, where Δt is the time step, $t_n = n\Delta t$, and $\hat{\omega}^n$ is the vorticity at time t_n .

$$\hat{\omega}^{n+1} = \hat{\omega}^n + \Delta t \left[\frac{3}{2} R(\hat{\omega}^n, t_n) - \frac{1}{2} R(\hat{\omega}^{n-1}, t_{n-1}) \right]. \quad (10)$$

B. Performance benchmark at different time steps

Since the model prediction errors are produced and accumulated at every step, prediction error increases dramatically with time due to the chaotic features of turbulence. Reducing the accumulated prediction errors on time dimension is therefore still one of the most challenging problems for surrogate models.

In this numerical experiment, we generate 1200 pairs of input-output data with the numerical solver, where each sample contains 20 steps of solutions of a random initialized condition at Reynolds number 10^5 . The solution is recorded every $t = 1$ time units. Both models (FNO, FNO+Attention) take the vorticity at previous 10 time steps solutions as input, and gives the vorticity at the next time step as output. During training, the vorticity of first 10 steps $\omega|_{(0,1)^2 \times [0,10]}$ is stacked over temporal dimension as the model input, and the model recurrently predicts the vorticity at the next step to fit the vorticity at next 10 steps $\omega|_{(0,1)^2 \times [11,20]}$, which are labeled as ground truth.

It is worth noting that the predicted vorticity at each step is recurrently treated as ground truth and reused as the inputs with the advance of time, thus the prediction errors are accumulated iteratively. We use 1000 samples for training and 200 samples for testing. After training, we evaluate both models on the test dataset, and compare their performance at three selected time steps ($t=11$, $t=15$, $t=20$). Fig. 5 compares the predicted vorticity and the absolute errors of a test sample: both models can accurately reconstruct the instantaneous spatial structures of turbulence in the beginning, however, the difference is enlarged significantly as time progresses. The FNO error increases at regions where the vorticity has dramatically changes. In contrast, the errors of attention-enhanced FNO are visibly smaller in terms of the region and magnitude. We find the same phenomenon in Fig.9 as we investigate the relative error ε of each time step. The relative error ε is defined by Eq. 11, where $\hat{\omega}$ is the predicted vorticity and ω is the ground truth vorticity.

$$\varepsilon = \frac{\|\hat{\omega} - \omega\|_2}{\|\omega\|_2}, \text{ where } \|x\|_2 = 1/n \sqrt{\sum_{k=1}^n |x_k|^2}. \quad (11)$$

The ensemble-averaged vorticity spectrum using 200 test samples $\overline{E_\omega(k)}$ is also compared in Fig.6: the predicted vorticity spectrum of both models can agree well with the ground truth in the low-wave number region. However, the FNO predicted spectrum deviates significantly from the ground truth at high-wave number region as time advances. In contrast, the attention enhanced model can accurately capture the small-scale flow structures and well reconstruct the vorticity spectrum at different flow scales. Fig.7 illustrates the PDFs of the normalized predicted vorticity on different time steps, where the vorticity is normalized by the root-mean-square values of ground truth vorticity. The predictions of both models have a good agreement with the ground truth in the beginning. However, as time advances, the predicted PDFs of both models become narrower, with the attention-enhanced FNO being closer to the ground truth.

Fig.8 shows the average of normalized absolute error conditioned on normalized vorticity at different time steps, where both vorticity and absolute error are normalized by the root-mean-square values of ground truth vorticity. We notice that the prediction errors of both models increase with the advance of time, and the attention-enhanced FNO achieves better performance with smaller error in the whole vorticity range. As can be seen from Fig.9, where the spatial-averaged relative

errors are plotted, the attention-enhanced model has achieved over 40% error reduction throughout all time steps.

C. Performance benchmark at different Reynolds numbers

Since the multi-scale flow structures become more chaotic and turbulent with the increasing of Reynolds numbers, reconstruction of turbulence at high Reynolds numbers has always been a challenging task for neural networks.

Table I shows the prediction relative errors (defined in Eq.11) of existing state-of-the-art neural network models including the FNO³⁴. Note that the results of U-Net⁴⁷, TF-Net³¹ and Resnet⁴⁸ are cited from reference³⁴. It is noted that all existing models perform well at low Reynolds number ($Re = 10^3$), and fails at higher Reynolds numbers ($Re = 10^4$ and $Re = 10^5$), with FNO achieving the lowest error. In contrast, the attention-enhanced FNO model further reduces the prediction errors of FNO by 40% at higher Reynolds numbers.

Here, we benchmark the prediction performance of FNO and attention-enhanced FNO, at the same time step ($t=15$), for different Reynolds numbers. We train and test both models on three groups of data where the flow Reynolds number is set to 10^3 , 10^4 , 10^5 respectively.

Fig.10 compares the snapshots of predicted vorticity and the absolute errors of the vorticity at different Reynolds numbers. Both models can accurately reconstruct the instantaneous spatial structures of turbulence at small Reynolds number $Re = 10^3$. However, when the flow becomes more turbulent at higher Reynolds numbers $Re = 10^4$ and 10^5 , the performance improvement of attention-enhanced FNO becomes more significant.

Fig.11 compares the ensemble-averaged vorticity spectrum of 200 test samples at different Reynolds numbers. At small Reynolds number $Re = 10^3$, both models can reconstruct the multi-scale flow statistics accurately. However, the vorticity spectrum predicted by FNO deviates away from the ground truth as the Reynolds number increases to $Re = 10^4$ and 10^5 . In comparison, the attention-enhanced FNO can accurately capture the flow statistics at different scales.

Fig.12 illustrates the PDFs of normalized predicted vorticity at different Reynolds numbers. At small Reynolds number ($Re = 10^3$), the predictions of both models have good agreements with the ground truth PDF. As the Reynolds number increases to $Re = 10^4$, the predicted PDFs of both models get narrower than the ground truth; and the gap is further enlarged as the Reynolds number increases to $Re = 10^5$.

Fig.13 shows the conditional average of normalized absolute error at different Reynolds numbers. The prediction errors of both models become larger as the Reynolds number increase from $Re = 10^3$ to $Re = 10^4$ and $Re = 10^5$, and the performance improvement of attention-enhanced FNO also becomes more obvious with the increasing of Reynolds numbers.

Fig.14 compares the mean and standard deviation of relative error on 200 test samples. Both models can achieve accurate predictions (1% error) at small Reynolds number

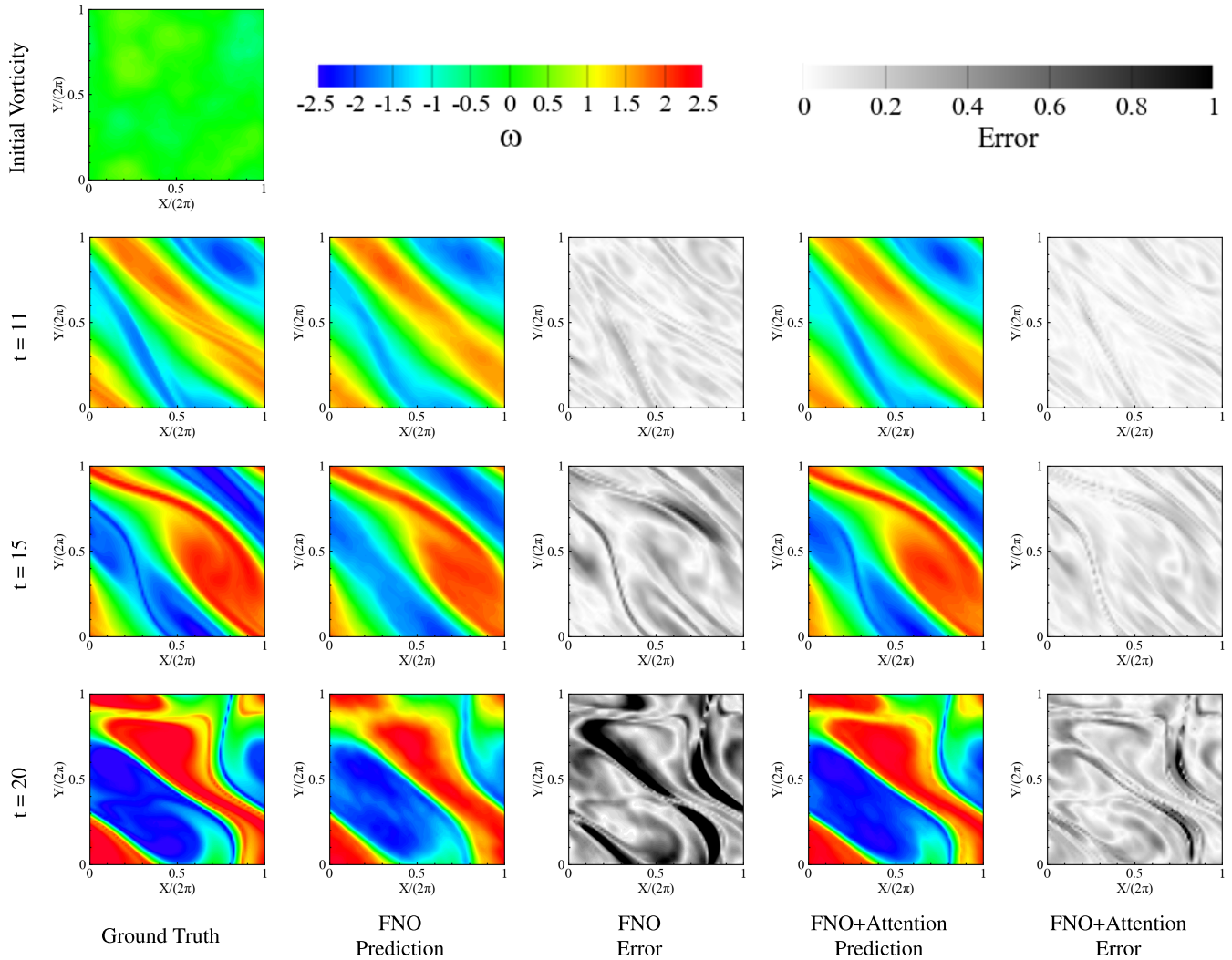


FIG. 5: Vorticity prediction and absolute error at selected time steps.

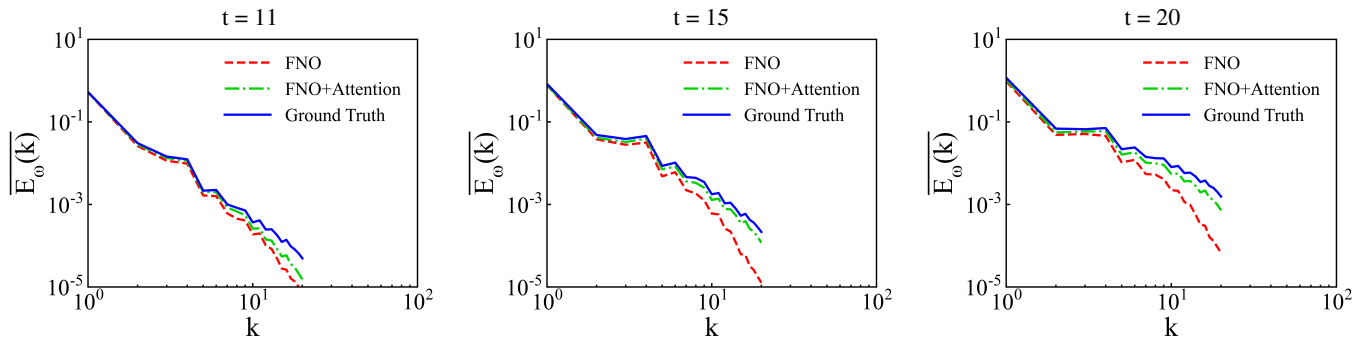


FIG. 6: Averaged vorticity spectrum on 200 test samples.

$Re = 10^3$; however, as the Reynolds number increases from 10^3 to 10^4 , the FNO prediction error arises from 1% to around 15%, whereas the FNO+Attention prediction error is about 8%; when the Reynolds number increases from 10^4 to 10^5 , the mean errors of both models are nearly unchanged except

that the error standard deviation becomes larger.

In addition to benchmark the approximation capacity of the two models, we also benchmark the model generalization ability across different Reynolds numbers. We train both models on $Re = 10^5$ dataset, and test the trained models on unseen

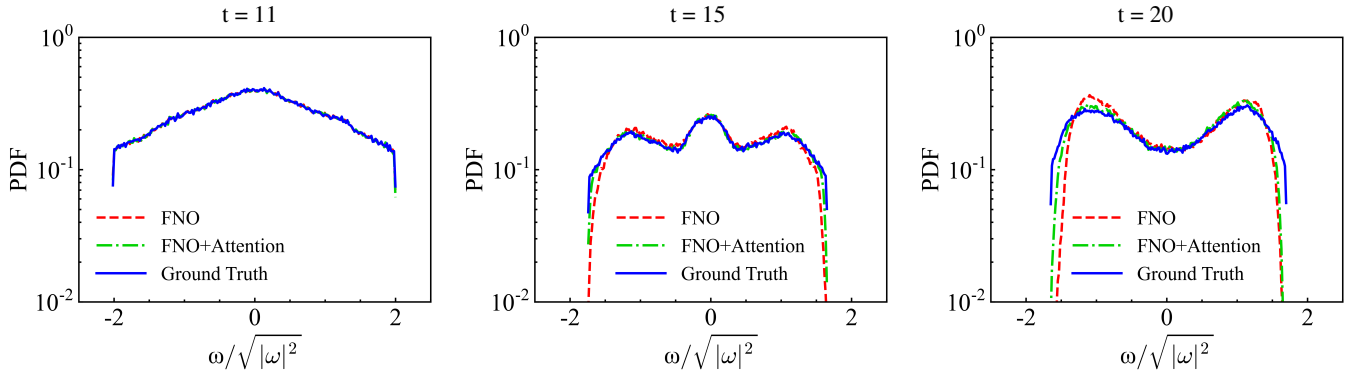


FIG. 7: PDF of normalized vorticity at different time steps.

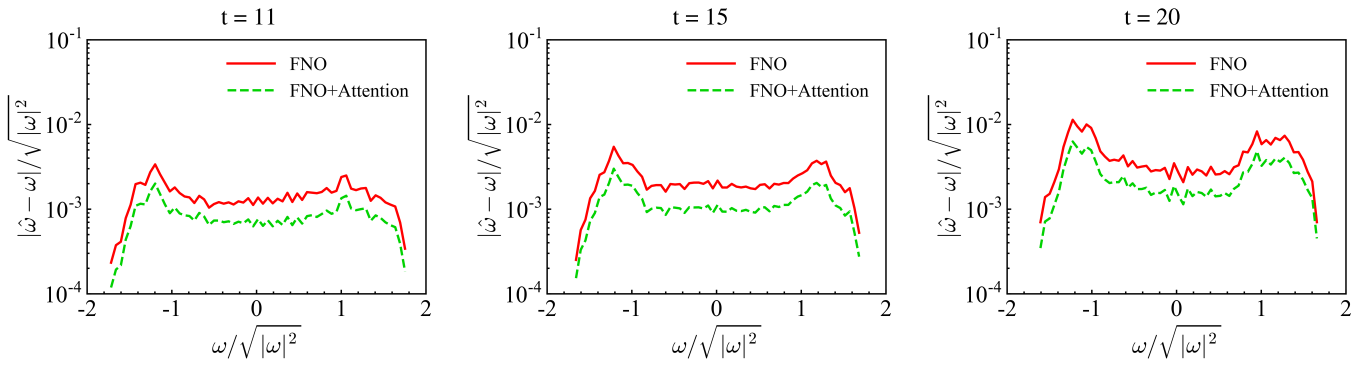
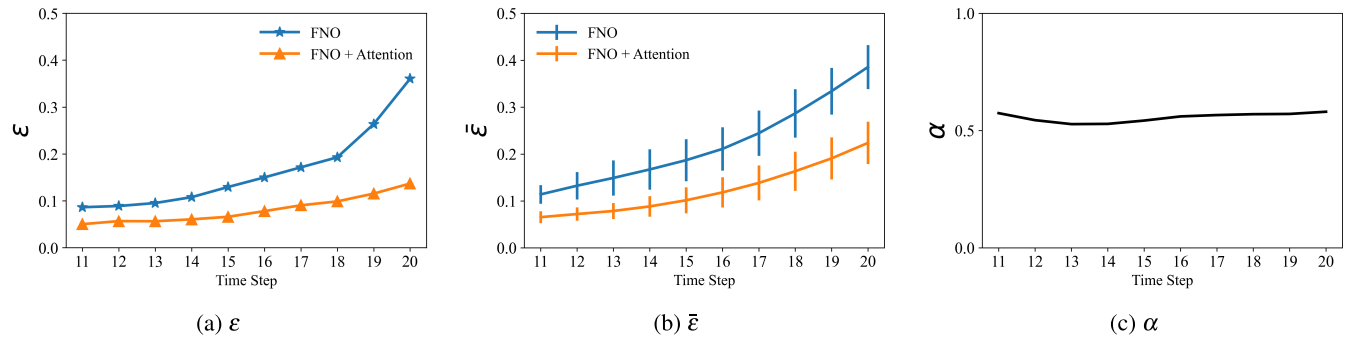


FIG. 8: Condition average error of vorticity at different time steps.



(a) Spatial-averaged relative error of vorticity on single test sample. (b) Spatial-averaged relative error of vorticity on 200 test samples. (c) Ratio of mean relative error.

FIG. 9: Relative error comparison at consequent time steps.

TABLE I: Prediction errors of neural network models at different Reynolds numbers

Model	Parameters	$Re = 10^3$	$Re = 10^4$	$Re = 10^5$
FNO + Attention	466,222	0.0096	0.0855	0.0864
FNO ³⁴	465,717	0.0094	0.1479	0.1507
U-Net ¹⁸	24,950,491	0.0245	0.2051	0.1982
TF-Net ³¹	7,451,724	0.0225	0.2253	0.2268
ResNet ⁴⁸	266,641	0.0701	0.2871	0.2753

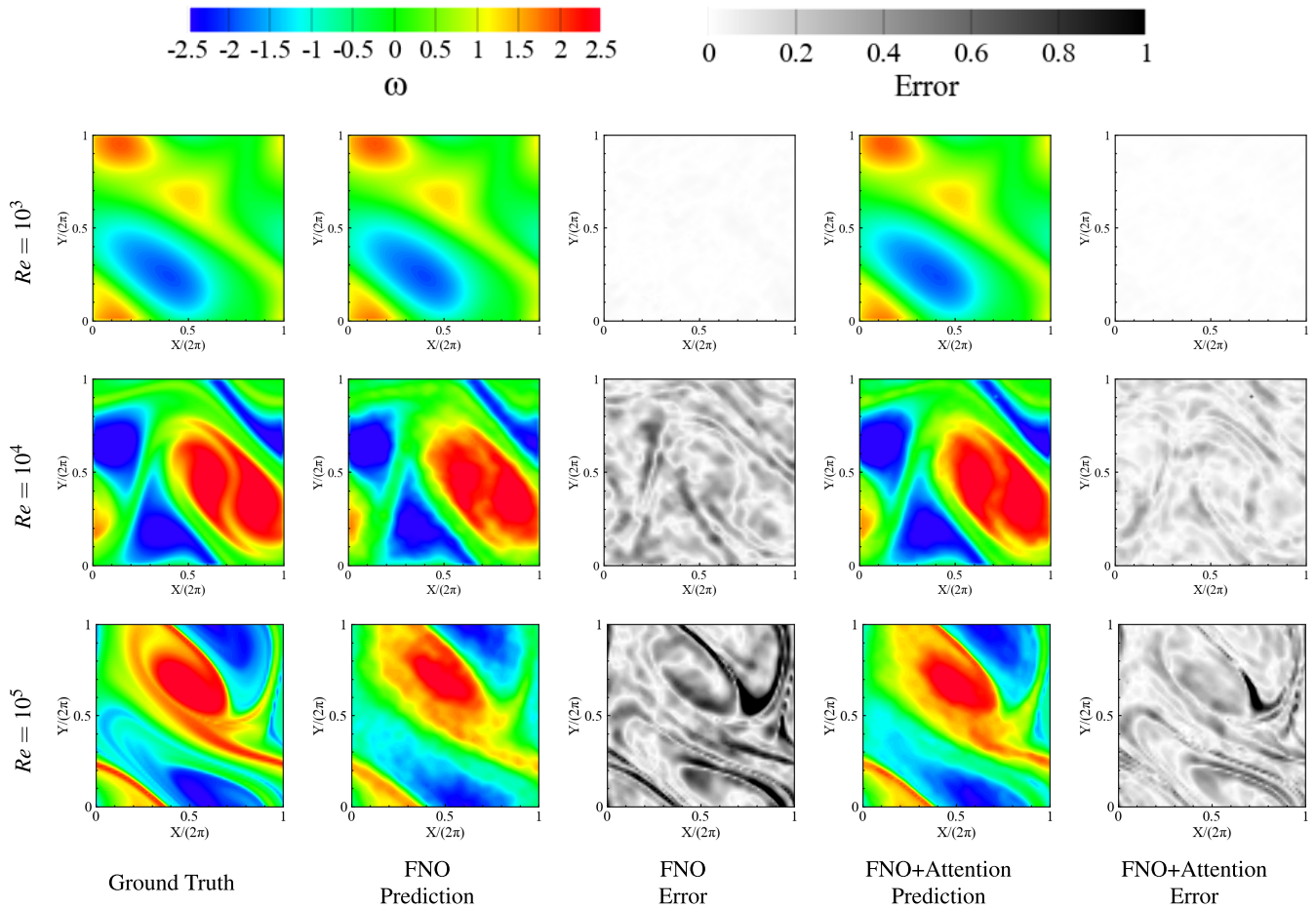


FIG. 10: Vorticity prediction and absolute error at different Reynolds numbers.

Reynolds numbers ranging from $Re = 10^3$ to $Re = 10^6$.

Fig.15 shows the generalization errors of FNO and attention-enhanced FNO models: both models can generalize well at high Reynolds numbers, whereas FNO generalizes better at low Reynolds numbers (below $Re = 5 \times 10^3$), and attention-enhanced FNO generalizes better at high Reynolds numbers. This result shows that the attention mechanism can capture the multi-scale characteristics of the high Reynolds numbers turbulence better as we expected.

Fig.16 shows the vorticity prediction and absolute error where the models are trained on $Re = 1 \times 10^5$ dataset and tested on three samples with different Reynolds numbers at $t = 15$. The test samples are initialized with the same random state, where the corresponding Reynolds numbers are set to $Re = 10^3$, $Re = 10^4$, and $Re = 10^6$ respectively. Both models fail to reconstruct the flow structures at low Reynolds number $Re = 10^3$, with FNO having smaller error than attention-enhanced FNO. By contrast, when the models are tested at high Reynolds numbers $Re = 10^4$ and $Re = 10^6$, the attention-enhanced FNO produces smaller generalization error than FNO, and can accurately reconstruct the multi-scale flow structures of turbulence.

D. Zero-shot super-resolution benchmark

The Fourier layers are discretization-invariant because they can learn from and evaluate functions which are discretized in an arbitrary way. Since parameters are learned directly in Fourier space, resolving the functions in physical space simply amounts to projecting on the basis $e^{2\pi i \langle x, k \rangle}$ which are well-defined everywhere on \mathbb{R}^d . This allows zero-shot super-resolution without losing accuracy³⁴. Such property provides free training acceleration and significant memory saving by training the model on the downsampled data.

Since the attention block, as shown in Fig.2, adopts 1×1 convolution, it retains the FNO mesh-invariant property. In this section, we benchmark the zero-shot super-resolution performance of two models. We generate data on grid size of 256×256 at the Reynolds number of 10^5 , then train both models on the downsampled data of grid size 64×64 . The trained models are evaluated at the same time step ($t=15$), on grid resolution of 64×64 , 128×128 and 256×256 , respectively.

Fig.17 shows the snapshots of predicted vorticity and the absolute errors at different grid resolutions. Unlike Figs.5 and 10 where the errors increase significantly with time steps and

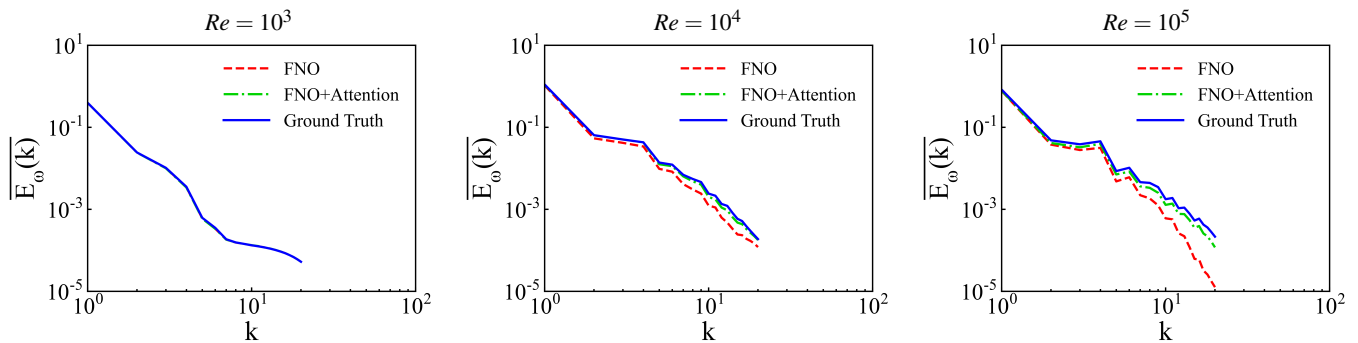


FIG. 11: Average spectrum at different Reynolds numbers.

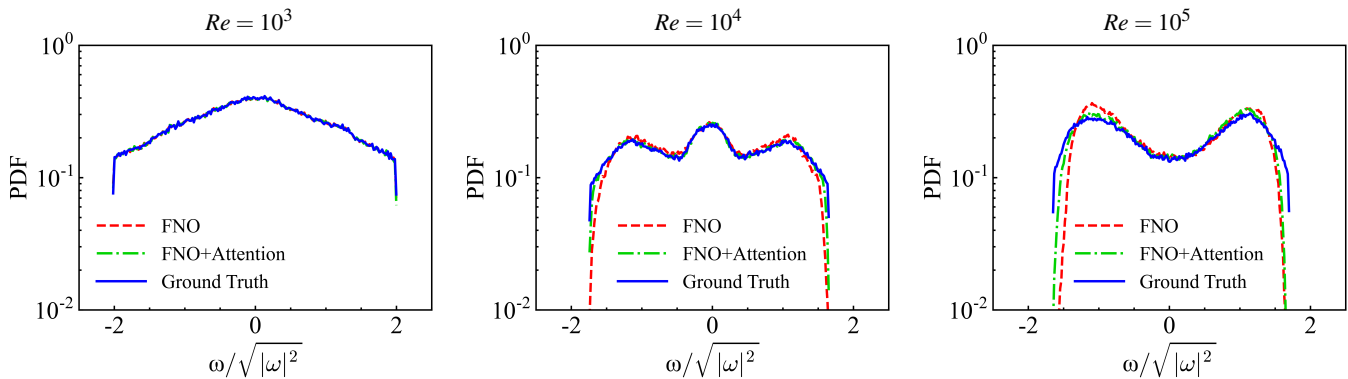


FIG. 12: PDF of normalized vorticity at different Reynolds numbers.

Reynolds numbers, the error rates of both models do not increase with grid size.

Fig. 18 compares the average relative error on different resolutions: both models have consistent error rates among different resolutions, whereas the attention-enhanced FNO achieves over 40% error reduction at all grid resolutions.

Fig. 19 compares the averaged vorticity spectrum of 200 test samples at different grid resolutions: the predicted vorticity spectrum of both models can agree well with the ground truth in low-wavenumber region. However, the FNO predicted spectrum deviates significantly from the ground truth at high-wavenumber region. In contrast, the FNO+Attention model can reconstruct the multi-scale flow structures accurately at all grid resolutions.

E. Performance benchmark on Taylor-Green turbulence and free shear turbulence

In this section, we benchmark the performance of different models on more challenging turbulence simulation tasks: the Taylor-Green turbulence and free shear turbulence. The Taylor-Green and free shear turbulence are governed by the same Navier-Stokes equations displayed in Eq. (6) without the forcing term. The Reynolds number is $Re = 10^3$ in both the Taylor-Green turbulence and free shear turbulence. The initial conditions of Taylor-Green and free shear turbulence

are given by Eq. 12 and Eq. 13 respectively^{49,50}.

$$\omega(\mathbf{x}, 0) = 2 \cos 2x_1 \cos 2x_2 + \lambda_1, \quad (12)$$

$$\omega(\mathbf{x}, 0) = 2\lambda_1 \cos 2x_1 + \delta\left(|x_2|, \frac{\pi}{2}\right) + \lambda_2. \quad (13)$$

Here, the magnitudes of perturbation λ_1 and λ_2 satisfy the Gaussian random distribution where $\lambda_1, \lambda_2 \sim \mathcal{N}(0, 10^{-3})$, and $\delta(a, b)$ is the Kronecker delta function, as described in Eq. 14.

$$\delta(a, b) = \begin{cases} 1 & \text{if } a = b \\ 0 & \text{otherwise} \end{cases} \quad (14)$$

Since it takes a long time for the Taylor-Green vortex to transition from the laminar flow to turbulence, we rotate the initial Taylor-Green vortex to a certain angle ($\theta \in (-10^\circ, 10^\circ)$) to break the symmetry of the base flow⁴⁹. We generate 1200 data samples on the grid size of 64×64 , where each sample contains 30 steps of solutions of a random initialized condition. Both models are trained on $t = 0$ to $t = 20$, and are tested on $t = 11$ to $t = 30$ to benchmark generalization performance on time dimension.

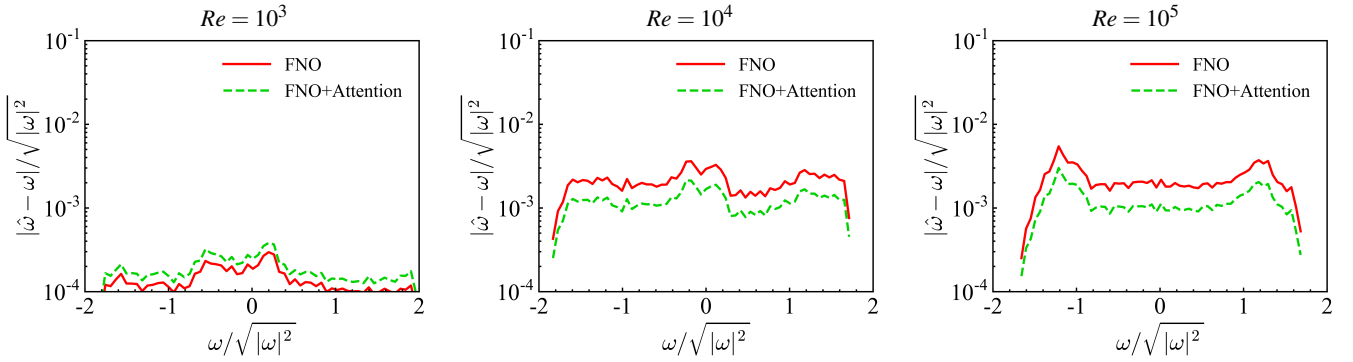


FIG. 13: Condition average error of vorticity at different Reynolds numbers.

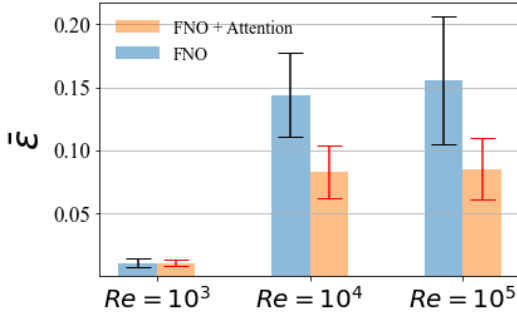


FIG. 14: Average relative error of vorticity at different Reynolds numbers.

Fig. 20 compares the predicted vorticity and the absolute errors on a test sample of Taylor-Green turbulence. The prediction errors of both models increase with the advance of time. At $t = 11$, both models can accurately reconstruct the instantaneous spatial structures of turbulence in the beginning; at $t = 20$, the attention-enhanced FNO can still make accurate reconstructions whereas the FNO cannot; at $t = 30$ where both models are tested on unseen time steps, the errors become too large for both models to perform accurate reconstructions.

Fig.21 shows the ensemble-averaged vorticity spectrum $\overline{E}_\omega(k)$ of Taylor-Green flow on 200 test samples. At $t = 11$, the predicted vorticity spectrum of FNO can agree well with the ground truth at low wave numbers, but deviates from the ground truth at high wave numbers; whereas the attention-enhanced FNO can well reconstruct the vorticity spectrum at different flow scales by accurately capturing small-scale flow structures. As time advances to $t = 20$, both models deviate further away from the ground truth at high-wave number region, with attention-enhanced FNO having better agreement with the ground truth. At $t = 30$, the predicted vorticity spectrum of FNO starts to deviate from the ground truth at low-wave number region too, whereas the predicted vorticity spectrum of attention-enhanced FNO does not.

Fig.22 compares the predicted vorticity and the absolute errors on a test sample of the free shear turbulence. The prediction errors of both models increase with the advance of time, with the errors of attention-enhanced FNO being significantly

smaller than FNO in terms of the region and magnitude. At $t = 11$ and $t = 20$, the attention-enhanced FNO captures the small-scale structures better than FNO, whereas both of them fail to reconstruct the instantaneous large-scale structures at $t = 30$.

Fig.23 presents the spatial-averaged relative errors of two models on predictions of the Taylor-Green turbulence and free shear turbulence. For the Taylor-Green turbulence, both models can generalize well on unseen time steps from $t = 21$ to $t = 30$; whereas for the free shear turbulence, the prediction errors increased significantly from $t = 21$ to $t = 30$, indicating that both models fail to generalize well on time dimension. In both Taylor-Green and free shear turbulence, the attention-enhanced FNO achieves 40% error reduction throughout all time steps.

V. DISCUSSION

A. Why does attention work ?

One of the most common criticisms that NNs often face is the lack of interpretability, therefore they are often treated as “black-box” surrogate models. Understanding how neural network based models make inference on physical problems requires future efforts from both data scientists and specialized experts of the area. We present some thoughts and ideas from the perspective of turbulence modeling, and leave them as an open discussion.

- We have investigated the FNO feature maps $v_t(\mathbf{x})$ and the attention refined feature maps $v_t(\mathbf{x})'$. These feature maps are the output of an intermediate layer, and they contain the information of how the neural networks understand turbulence. The feature maps are stacked together and are characterized by a 3-dimensional metrics ($C \times S \times S$), where C is the channel dimension and S is the grid size. The value of the channel dimension equals to the number of convolution filters used in the Fourier layer (20 in this work). Fig.24 shows the unfolded feature maps of each channels. We noticed that the features learned by FNO are relatively uniformly distributed in

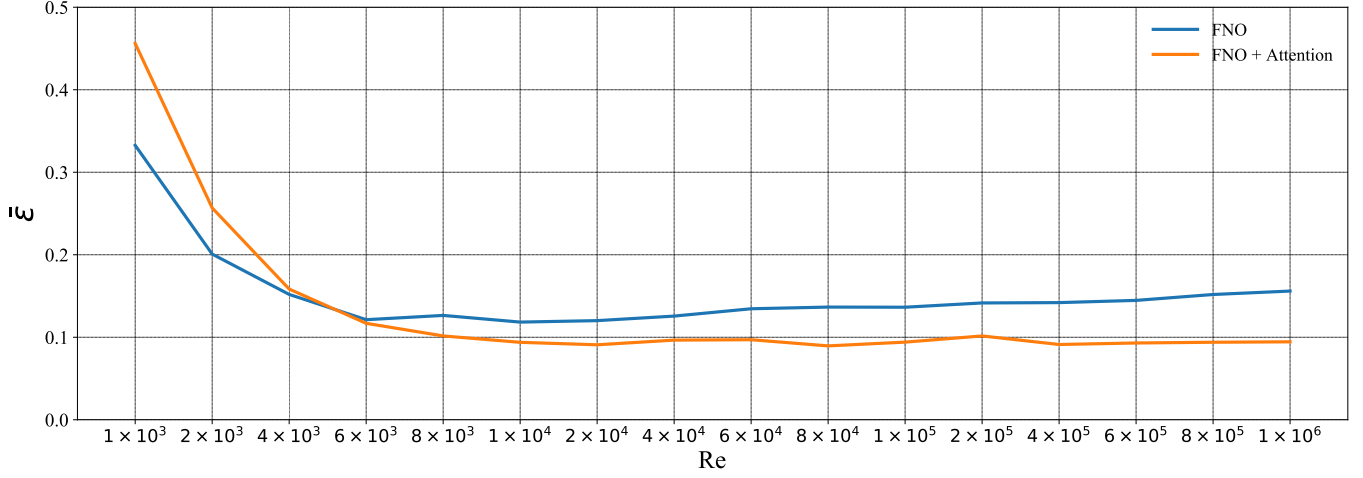


FIG. 15: Generalization error at different Reynolds numbers (models trained on $Re = 1 \times 10^5$ dataset).

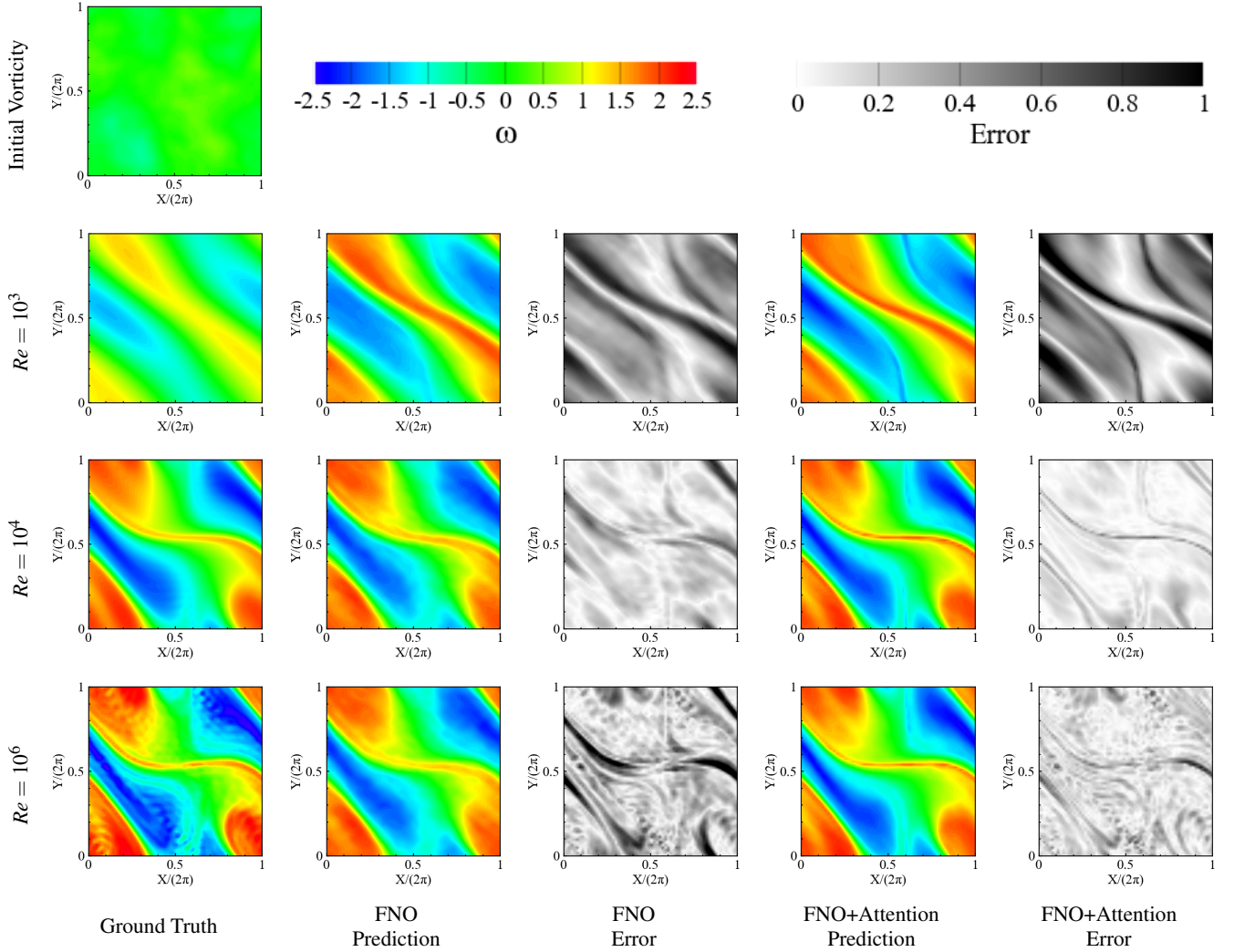


FIG. 16: Vorticity prediction and absolute error at different Reynolds numbers. (models trained on $Re = 1 \times 10^5$ dataset).

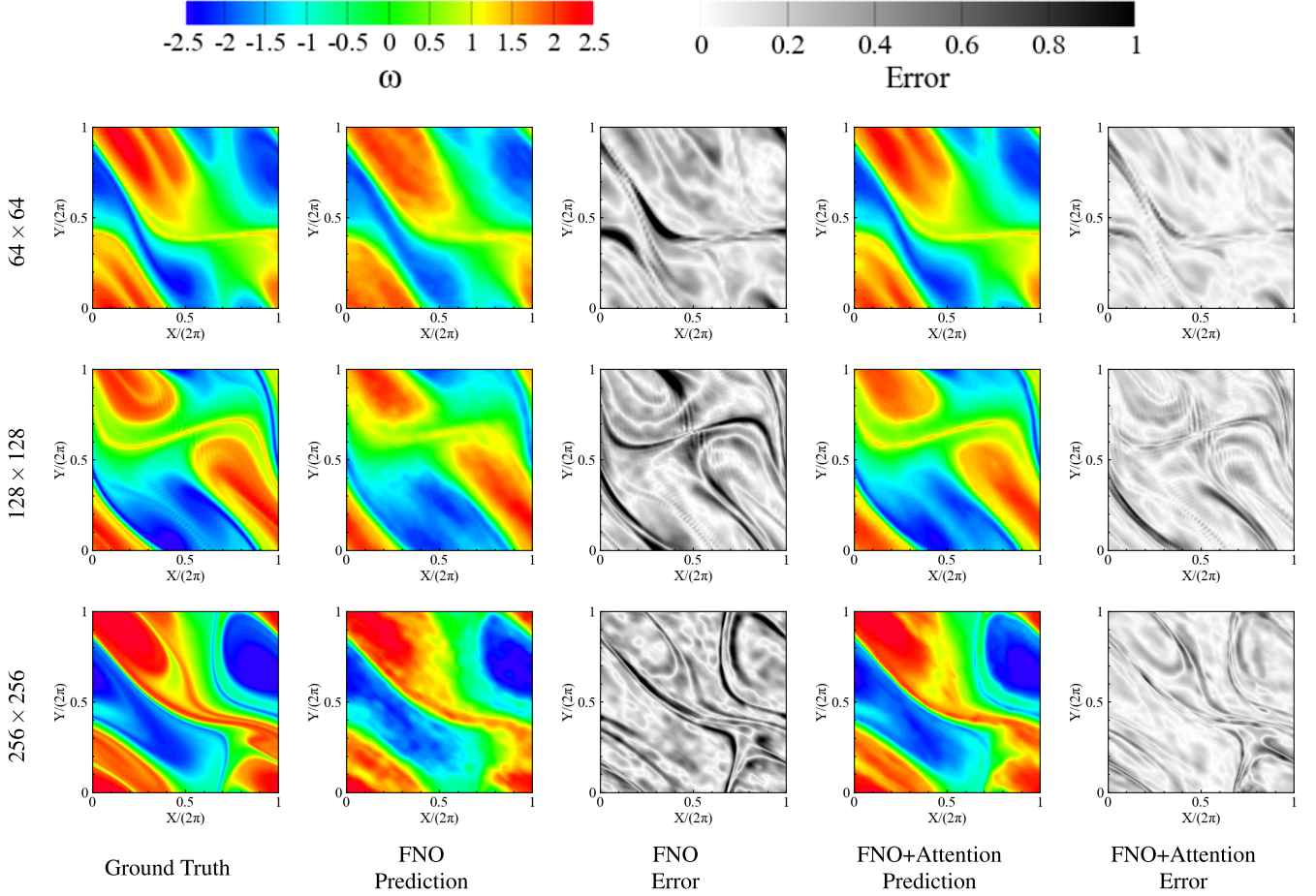


FIG. 17: Vorticity prediction and absolute error at different resolutions.

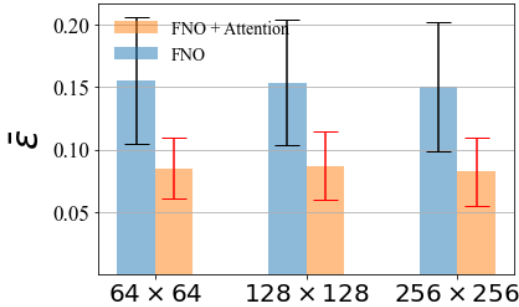


FIG. 18: Average relative error at different resolutions.

space, whereas the attention refined features are not. Moreover, the attention refined feature maps are visually similar to the vorticity distribution, indicating that attention module can capture the turbulence nonequilibrium features better as we expected.

- Another interesting phenomenon is that the large error is closely related with the regions where the vorticity changes dramatically, as shown in Fig.5. We therefore

investigate the relationship between the absolute error $|\hat{\omega} - \omega|$ and vorticity gradient $\nabla\omega$, as shown in Fig.25. We noticed that the errors of both models grow with the increasing of vorticity gradient. Further improvements can be made by adding an extra vorticity gradient penalty term with the loss function during training.

B. Computational efficiency

Table II compares computational cost of 10 prediction steps on a 64×64 grid using 3 different approaches. These numerical experiments are ran on a virtual machine powered by Google Colab, where the CPU type is Intel(R) Xeon(R) CPU @ 2.30GHz and GPU type is Tesla K80. Once trained, the surrogate models can be extremely efficient compared with traditional approaches. Both models provide 8000 folds speedup compared with the pseudo-spectral numerical solver. The attention-augmented neural network model achieves 40% error reduction at the same level of memory consuming and computational expense.

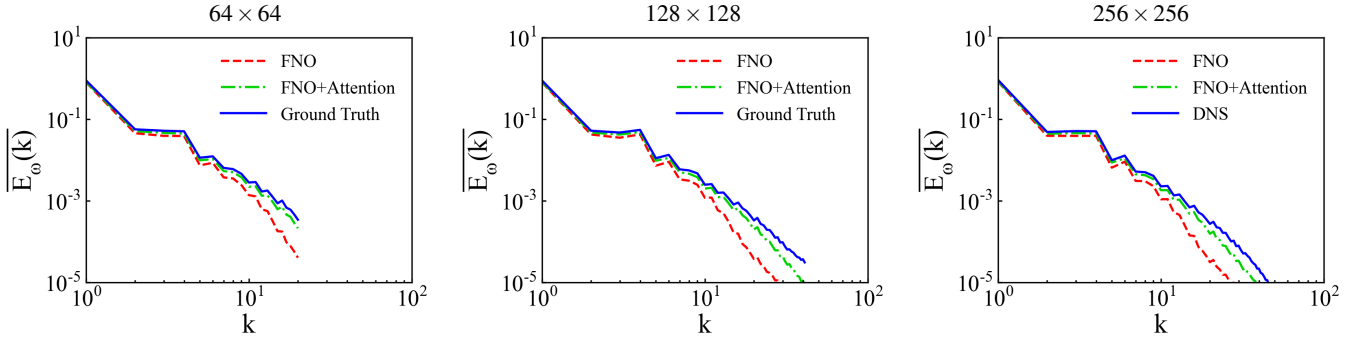


FIG. 19: Average spectrum of vorticity at different resolutions.

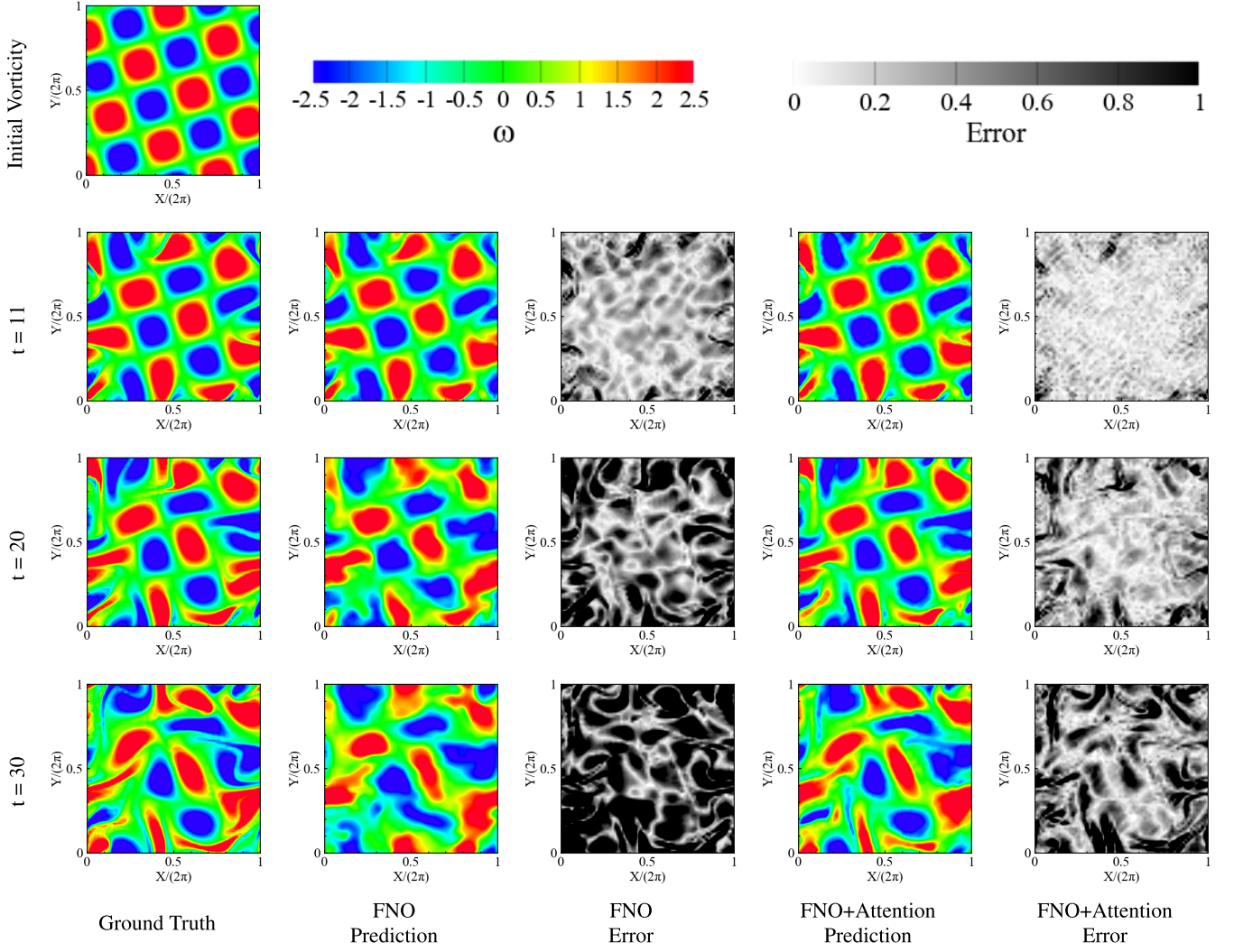


FIG. 20: Vorticity prediction and absolute error at selected time steps (Taylor-Green turbulence).

VI. CONCLUSION

In this work, we propose an attention-enhanced neural network approach to model the nonequilibrium feature of tur-

bulence. Numerical experiments show that: 1) the proposed model can significantly reduce the prediction error induced by temporal accumulation, and can accurately reconstruct the instantaneous spatial structures of turbulence. 2) the attention-enhanced FNO model can reduce the prediction error rate by

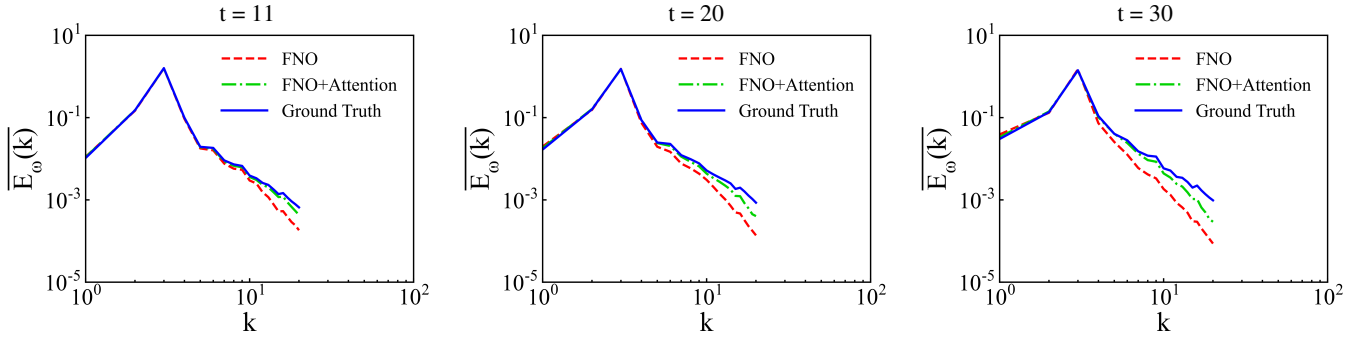


FIG. 21: Averaged vorticity spectrum on 200 test samples (Taylor-Green turbulence).

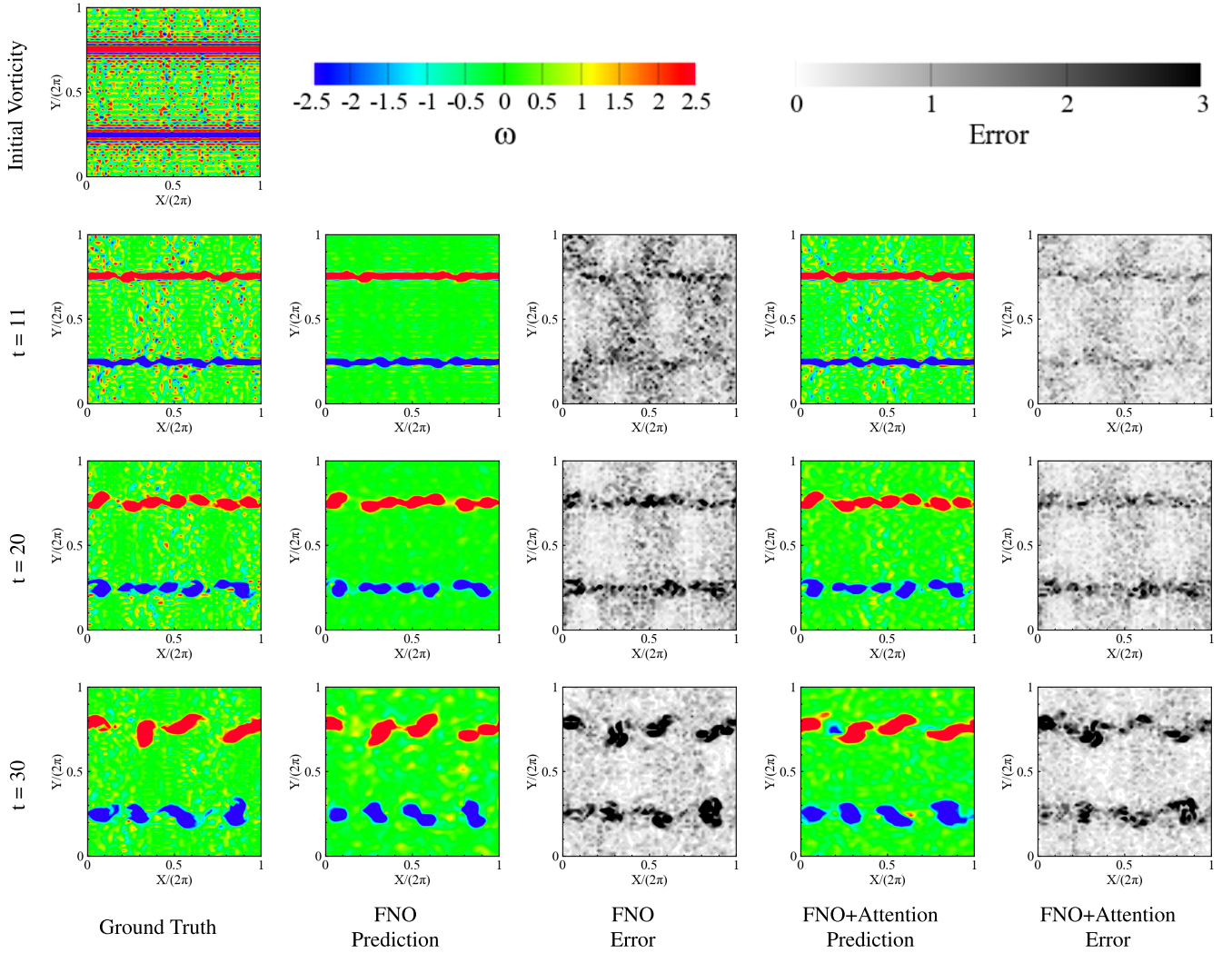
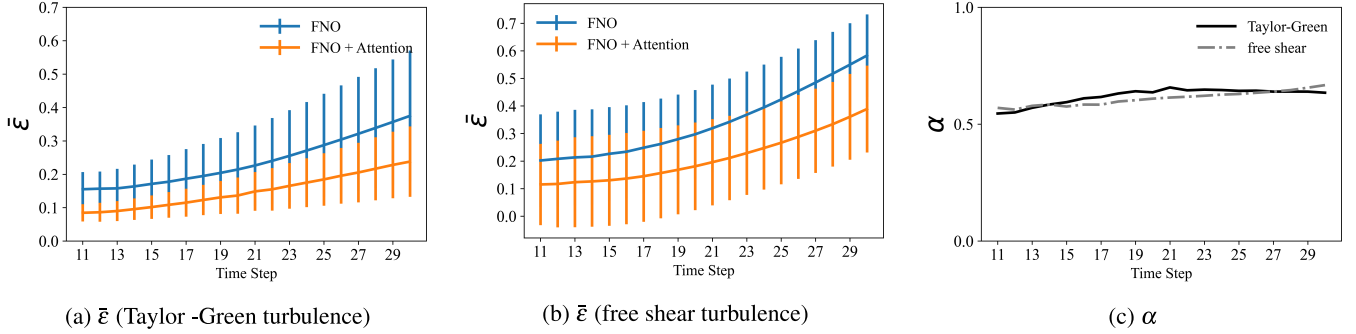


FIG. 22: Vorticity prediction and absolute error at selected time steps (free shear turbulence).

40% as the flow becomes more turbulent at higher Reynolds numbers. 3) the attention-enhanced model retains the mesh-invariant property of FNO: the FNO+Attention model can be trained on lower grid resolution and evaluated on higher grid resolution, without losing accuracy. 4) The attention enhanced

FNO model achieves the same level of computational efficiency as compared with the original FNO model.



(a) Spatial-averaged relative error of vorticity on 200 test samples (Taylor-Green turbulence). (b) Spatial-averaged relative error of vorticity on 200 test samples (free shear turbulence). (c) Ratios of mean relative error.

FIG. 23: Relative error comparison at consequent time steps.

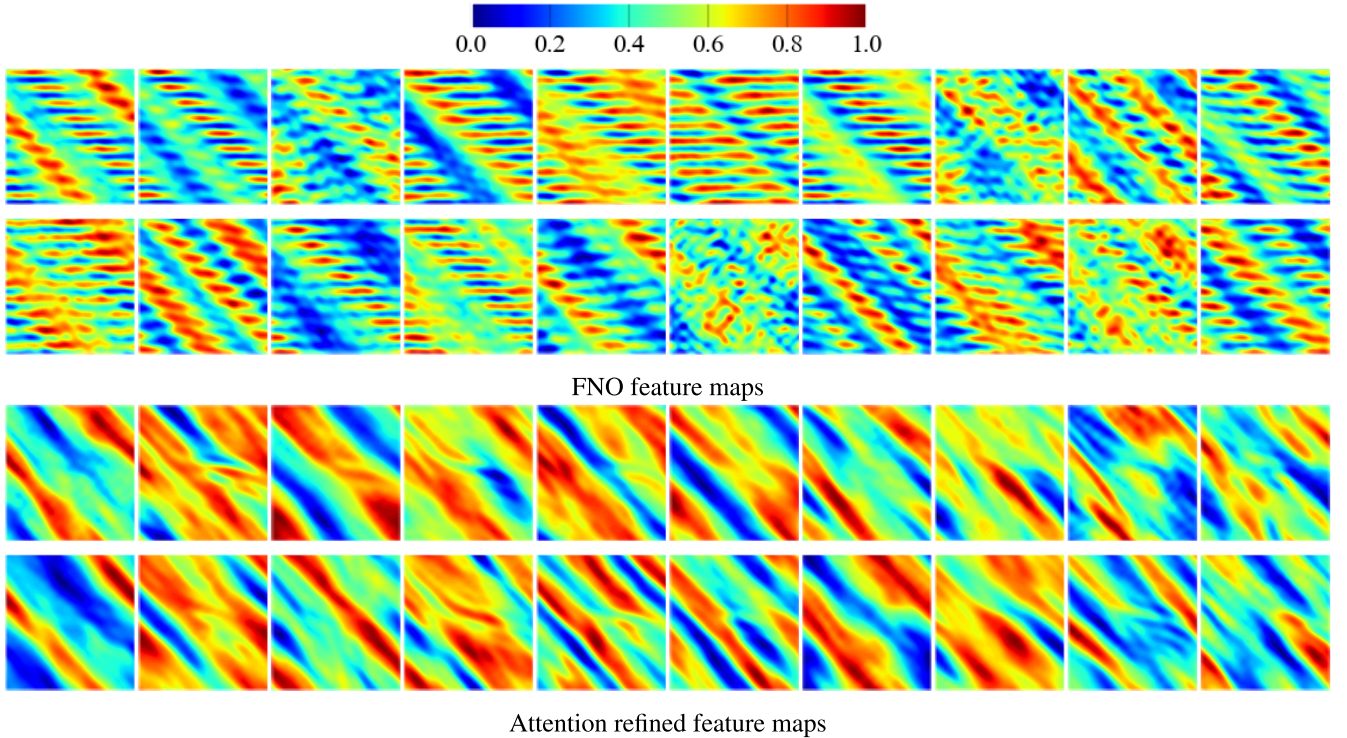


FIG. 24: Comparison of feature maps.

Method	Parameters	GPU Timing
Numerical Solver	N/A	502.85s
FNO	465,717	0.0579s
FNO + Attention	466,222	0.0587s

TABLE II: Computational efficiency comparison of three different numerical approaches.

VII. DATA AVAILABILITY

The data that support the findings of this study are available from the corresponding author upon reasonable request.

ACKNOWLEDGMENTS

This work was supported by the National Natural Science Foundation of China (NSFC Grant Nos. 91952104, 92052301, 12172161 and 91752201), by the National Numerical Windtunnel Project (No.NNW2019ZT1-A04), by the Shenzhen Science and Technology Program (Grants No.KQTD20180411143441009), by Key Special Project for Introduced Talents Team of Southern Marine Science and Engineering Guangdong Laboratory (Guangzhou) (Grant No. GML2019ZD0103), by CAAI-Huawei MindSpore Open Fund, and by Department of Science and Technology of Guangdong Province (No.2020B1212030001). This work

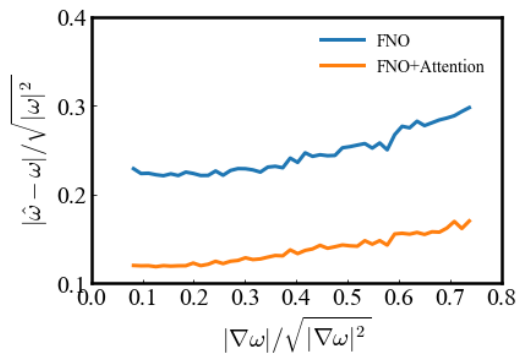


FIG. 25: Normalized absolute error versus normalized vorticity gradient.

was also supported by Center for Computational Science and Engineering of Southern University of Science and Technology.

- ¹S. L. Brunton, B. R. Noack, and P. Koumoutsakos, “Machine learning for fluid mechanics,” *Annual Review of Fluid Mechanics* **52**, 477–508 (2020).
- ²K. Duraisamy, G. Iaccarino, and H. Xiao, “Turbulence modeling in the age of data,” *Annual Review of Fluid Mechanics* **51**, 357–377 (2019).
- ³J. Ling, A. Kurzawski, and J. Templeton, “Reynolds averaged turbulence modelling using deep neural networks with embedded invariance,” *Journal of Fluid Mechanics* **807**, 155–166 (2016).
- ⁴R. Maulik, O. San, A. Rasheed, and P. Vedula, “Subgrid modelling for two-dimensional turbulence using neural networks,” *Journal of Fluid Mechanics* **858**, 122–144 (2019).
- ⁵Y. Wang, Z. Yuan, C. Xie, and J. Wang, “Artificial neural network-based spatial gradient models for large-eddy simulation of turbulence,” *AIP Advances* **11**, 055216 (2021).
- ⁶A. Beck, D. Flad, and C.-D. Munz, “Deep neural networks for data-driven les closure models,” *Journal of Computational Physics* **398**, 108910 (2019).
- ⁷G. D. Portwood, B. T. Nadiga, J. A. Saenz, and D. Livescu, “Interpreting neural network models of residual scalar flux,” *Journal of Fluid Mechanics* **907** (2021).
- ⁸J. Park and H. Choi, “Toward neural-network-based large eddy simulation: application to turbulent channel flow,” *Journal of Fluid Mechanics* **914** (2021).
- ⁹Z. Yuan, Y. Wang, C. Xie, and J. Wang, “Dynamic iterative approximate deconvolution models for large-eddy simulation of turbulence,” *Physics of Fluids* **33**, 085125 (2021).
- ¹⁰D. Kochkov, J. A. Smith, A. Alieva, Q. Wang, M. P. Brenner, and S. Hoyer, “Machine learning–accelerated computational fluid dynamics,” *Proceedings of the National Academy of Sciences* **118** (2021).
- ¹¹B. Lusch, J. N. Kutz, and S. L. Brunton, “Deep learning for universal linear embeddings of nonlinear dynamics,” *Nature communications* **9**, 1–10 (2018).
- ¹²J. Sirignano and K. Spiliopoulos, “Dgm: A deep learning algorithm for solving partial differential equations,” *Journal of computational physics* **375**, 1339–1364 (2018).
- ¹³H. Tang, L. Li, M. Grossberg, Y. Liu, Y. Jia, S. Li, and W. Dong, “An exploratory study on machine learning to couple numerical solutions of partial differential equations,” *Communications in Nonlinear Science and Numerical Simulation* **97**, 105729 (2021).
- ¹⁴Y. Sun, L. Zhang, and H. Schaeffer, “Neupde: Neural network based ordinary and partial differential equations for modeling time-dependent data,” in *Mathematical and Scientific Machine Learning* (PMLR, 2020) pp. 352–372.
- ¹⁵Z. Li, N. Kovachki, K. Azizzadenesheli, B. Liu, K. Bhattacharya, A. Stuart, and A. Anandkumar, “Neural operator: Graph kernel network for partial differential equations,” arXiv preprint arXiv:2003.03485 (2020).
- ¹⁶X. Jin, P. Cheng, W.-L. Chen, and H. Li, “Prediction model of velocity field around circular cylinder over various reynolds numbers by fusion convolutional neural networks based on pressure on the cylinder,” *Physics of Fluids* **30**, 047105 (2018).
- ¹⁷V. Sekar, Q. Jiang, C. Shu, and B. C. Khoo, “Fast flow field prediction over airfoils using deep learning approach,” *Physics of Fluids* **31**, 057103 (2019).
- ¹⁸J. Chen, J. Viquerat, and E. Hachem, “U-net architectures for fast prediction of incompressible laminar flows,” arXiv preprint arXiv:1910.13532 (2019).
- ¹⁹C. Cheng and G.-T. Zhang, “Deep learning method based on physics-informed neural network with resnet block for solving fluid flow problems,” *Water* **13**, 423 (2021).
- ²⁰M. Z. Yousif, L. Yu, and H.-C. Lim, “High-fidelity reconstruction of turbulent flow from spatially limited data using enhanced super-resolution generative adversarial network,” *Physics of Fluids* **33**, 125119 (2021).
- ²¹J. Chen, E. Hachem, and J. Viquerat, “Graph neural networks for laminar flow prediction around random two-dimensional shapes,” *Physics of Fluids* **33**, 123607 (2021).
- ²²D. Schmidt, R. Maulik, and K. Lyras, “Machine learning accelerated turbulence modeling of transient flashing jets,” *Physics of Fluids* **33**, 127104 (2021).
- ²³R. Han, Y. Wang, Y. Zhang, and G. Chen, “A novel spatial-temporal prediction method for unsteady wake flows based on hybrid deep neural network,” *Physics of Fluids* **31**, 127101 (2019).
- ²⁴H. Wang, Z. Yang, B. Li, and S. Wang, “Predicting the near-wall velocity of wall turbulence using a neural network for particle image velocimetry,” *Physics of Fluids* **32**, 115105 (2020).
- ²⁵Y. Li, J. Chang, Z. Wang, and C. Kong, “An efficient deep learning framework to reconstruct the flow field sequences of the supersonic cascade channel,” *Physics of Fluids* **33**, 056106 (2021).
- ²⁶J. Ren, H. Wang, G. Chen, K. Luo, and J. Fan, “Predictive models for flame evolution using machine learning: A priori assessment in turbulent flames without and with mean shear,” *Physics of Fluids* **33**, 055113 (2021).
- ²⁷M. Raissi, P. Perdikaris, and G. E. Karniadakis, “Physics-informed neural networks: A deep learning framework for solving forward and inverse problems involving nonlinear partial differential equations,” *Journal of Computational Physics* **378**, 686–707 (2019).
- ²⁸N. B. Erichson, M. Muehlebach, and M. W. Mahoney, “Physics-informed autoencoders for lyapunov-stable fluid flow prediction,” arXiv preprint arXiv:1905.10866 (2019).
- ²⁹S. Pawar, O. San, A. Nair, A. Rasheed, and T. Kvamsdal, “Model fusion with physics-guided machine learning: Projection-based reduced-order modeling,” *Physics of Fluids* **33**, 067123 (2021).
- ³⁰H. Xu, W. Zhang, and Y. Wang, “Explore missing flow dynamics by physics-informed deep learning: The parameterized governing systems,” *Physics of Fluids* **33**, 095116 (2021).
- ³¹R. Wang, K. Kashinath, M. Mustafa, A. Albert, and R. Yu, “Towards physics-informed deep learning for turbulent flow prediction,” in *Proceedings of the 26th ACM SIGKDD International Conference on Knowledge Discovery & Data Mining* (2020) pp. 1457–1466.
- ³²Y. Fan, C. O. Bohorquez, and L. Ying, “Bcr-net: A neural network based on the nonstandard wavelet form,” *Journal of Computational Physics* **384**, 1–15 (2019).
- ³³K. Kashinath, P. Marcus, *et al.*, “Enforcing physical constraints in cnns through differentiable pde layer,” in *ICLR 2020 Workshop on Integration of Deep Neural Models and Differential Equations* (2020).
- ³⁴Z. Li, N. Kovachki, K. Azizzadenesheli, B. Liu, K. Bhattacharya, A. Stuart, and A. Anandkumar, “Fourier neural operator for parametric partial differential equations,” arXiv preprint arXiv:2010.08895 (2020).
- ³⁵D. Bahdanau, K. Cho, and Y. Bengio, “Neural machine translation by jointly learning to align and translate,” arXiv preprint arXiv:1409.0473 (2014).
- ³⁶A. Vaswani, N. Shazeer, N. Parmar, J. Uszkoreit, L. Jones, A. N. Gomez, L. Kaiser, and I. Polosukhin, “Attention is all you need,” in *Advances in neural information processing systems* (2017) pp. 5998–6008.
- ³⁷N. Parmar, A. Vaswani, J. Uszkoreit, L. Kaiser, N. Shazeer, A. Ku, and D. Tran, “Image transformer,” in *International Conference on Machine Learning* (PMLR, 2018) pp. 4055–4064.
- ³⁸X. Liu and M. Milanova, “Visual attention in deep learning: a review,” *Int Rob Auto J* **4**, 154–155 (2018).

- ³⁹P. Wu, S. Gong, K. Pan, F. Qiu, W. Feng, and C. Pain, “Reduced order model using convolutional auto-encoder with self-attention,” *Physics of Fluids* **33**, 077107 (2021).
- ⁴⁰S. Pan and K. Duraisamy, “Physics-informed probabilistic learning of linear embeddings of nonlinear dynamics with guaranteed stability,” *SIAM Journal on Applied Dynamical Systems* **19**, 480–509 (2020).
- ⁴¹K. Wu and D. Xiu, “Data-driven deep learning of partial differential equations in modal space,” *Journal of Computational Physics* **408**, 109307 (2020).
- ⁴²H. Xu, D. Zhang, and J. Zeng, “Deep-learning of parametric partial differential equations from sparse and noisy data,” *Physics of Fluids* **33**, 037132 (2021).
- ⁴³B. Beauzamy, *Introduction to Banach spaces and their geometry* (Elsevier, 2011).
- ⁴⁴V. N. Vapnik, “An overview of statistical learning theory,” *IEEE transactions on neural networks* **10**, 988–999 (1999).
- ⁴⁵H. Zhang, I. Goodfellow, D. Metaxas, and A. Odena, “Self-attention generative adversarial networks,” in *International conference on machine learning* (PMLR, 2019) pp. 7354–7363.
- ⁴⁶G. J. Kowalski, *Information retrieval systems: theory and implementation*, Vol. 1 (Springer, 2007).
- ⁴⁷O. Ronneberger, P. Fischer, and T. Brox, “U-net: Convolutional networks for biomedical image segmentation,” in *International Conference on Medical image computing and computer-assisted intervention* (Springer, 2015) pp. 234–241.
- ⁴⁸K. He, X. Zhang, S. Ren, and J. Sun, “Deep residual learning for image recognition,” in *Proceedings of the IEEE conference on computer vision and pattern recognition* (2016) pp. 770–778.
- ⁴⁹O. San and R. Maulik, “Stratified kelvin–helmholtz turbulence of compressible shear flows,” *Nonlinear Processes in Geophysics* **25**, 457–476 (2018).
- ⁵⁰T. K. Sengupta, N. Sharma, and A. Sengupta, “Non-linear instability analysis of the two-dimensional navier-stokes equation: The taylor-green vortex problem,” *Physics of Fluids* **30**, 054105 (2018).